Electronic Poiseuille flow in hexagonal boron nitride encapsulated graphene field effect transistors

Wenhao Huang,[1,2,*] Tathagata Paul,[1,*,†] Kenji Watanabe,[3] Takashi Taniguchi,[4] Mickael L. Perrin,[1,5,‡] and Michel Calame[1,2,6,§]

[1]*Empa, Swiss Federal Laboratories for Materials Science and Technology, Transport at Nanoscale Interfaces Laboratory, Überlandstrasse 129, CH-8600 Dübendorf, Switzerland*

[2]*Department of Physics, University of Basel, Klingelbergstrasse 82, CH-4056 Basel, Switzerland*

[3]*Research Center for Functional Materials, National Institute for Materials Science, 1-1 Namiki, Tsukuba, Ibaraki 305-0044, Japan*

[4]*International Center for Materials Nanoarchitectonics, National Institute for Materials Science, 1-1 Namiki, Tsukuba, Ibaraki 305-0044, Japan*

[5]*Department of Information Technology and Electrical Engineering, ETH Zürich, 8092 Zürich, Switzerland*

[6]*Swiss Nanoscience Institute, University of Basel, Klingelbergstrasse 82, CH-4056 Basel, Switzerland*

Electron-electron interactions in graphene are sufficiently strong to induce a correlated and momentum-conserving flow such that charge carriers behave similarly to the Hagen-Poiseuille flow of a classical fluid. In the current work, we investigate the electronic signatures of such a viscous charge flow in high-mobility graphene field effect transistors (FETs). In two complementary measurement schemes, we monitor differential resistance of graphene for different channel widths and for different effective electron temperatures. By combining both approaches, the presence of viscous effects is verified in a temperature range starting from 178 K and extending up to room temperature. Our experimental findings are supported by finite element calculations of the graphene channel, which also provide design guidelines for device geometries that exhibit increased viscous effects. The presence of viscous effects near room temperature opens up avenues for functional hydrodynamic devices such as geometric rectifiers like a Tesla valve and charge amplifiers based on the electronic Venturi effect.

I. INTRODUCTION

The dynamics governing the flow of charges in conductors is heavily dependent on the ratios of the different physical length scales present in the system. These length scales dictate how the charge carriers interact with each other, with the system boundaries, and with defects or impurities. Microscopically, the flow of charge carriers is resisted by scattering from defects and lattice vibrations (phonons), characterized by the length scale l_{diff}, which is the average distance traveled by the charge carriers between two such momentum-relaxing scattering events. The charge carriers also interact with each other in a momentum-conserving fashion, with a length scale l_{ee}. The third relevant length scale is the channel width w (assuming channel length $l \gg w$), dictating how often charge carriers interact with the boundary of the system.

In most conductors, diffusive scattering prevails ($l_{\text{diff}} < l_{ee}, w$) and charge transport is Ohmic. Charge carriers traveling across the channel suffer many momentum relaxing collisions leading to a constant drift velocity along the direction of the applied electric field [1]. Alternatively, transport is ballistic, when the channel dimensions are the smallest length scale in the system. Under these circumstances, charge carriers travel collision-less from the source to the drain terminal, dissipating energy only at the contacts [2]. However, a third, and relatively unexplored transport regime emerges, when interparticle scattering dominates ($l_{ee} < l_{\text{diff}}, w$). These strong interparticle interactions lead to a correlated, viscous charge flow, similar to the flow of fluids and governed by the theory of hydrodynamics [3–10]. A direct consequence of this behavior is the nonuniformity of the carrier velocity in the channel, which follows a Poiseuille-like flow profile, similar to fluids [Fig. 1(a)]. In the context of electrical transport, this translates to a (nonuniform) position-dependent current density, being largest in the center of the channel and decreasing on approaching the channel edges, following a parabolic profile.

Fulfilling the criteria of charge hydrodynamics requires high-mobility devices with reduced scattering from defects and phonons (large l_{diff}) and strong interparticle interactions (small l_{ee}). Graphene fulfills both these requirements. First, the electron-electron interaction strength is enhanced due to the 2D confinement effects and weaker mutual screening of charges in graphene when compare to metals (small l_{ee}) [11,12]. Second, graphene has a weak electron-phonon coupling strength [13–15] and advancements in fabrication

*These authors contributed equally to this work.

†tathagata.paul@empa.ch

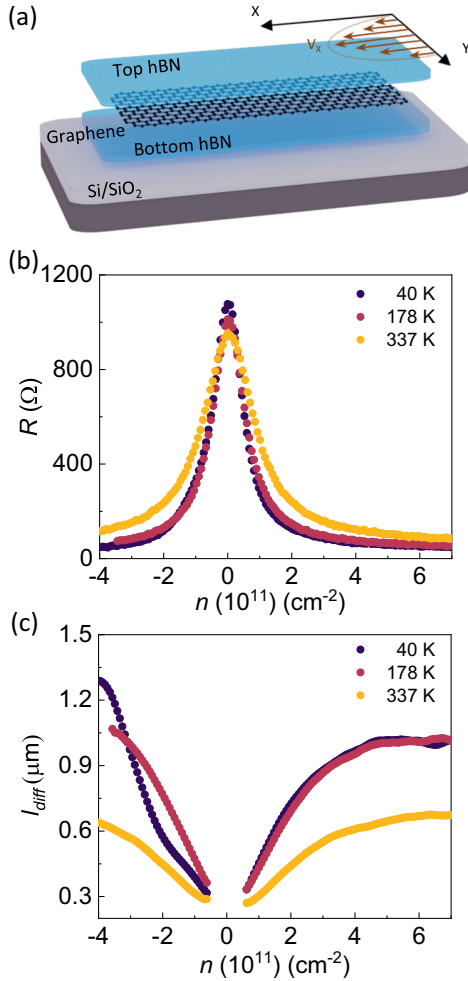‡Mickael.Perrin@empa.ch

§michel.calame@empa.ch

FIG. 1. Device structure and electrical performance. (a) Schematic depiction of the graphene heterostructure used in the current work. The Poiseuille flow profile is depicted above the top *h*-BN. The arrows and the curve represent the particle velocity and the velocity profile expected for Poiseuille flow, respectively. (b) Transfer characteristics of a typical GrFET device at different values of T. (c) Diffusive scattering length scale (l_{diff}) of GrFET device extracted from the transfer characteristics in (b).

techniques make it possible to limit scattering from extrinsic disorders, in particular by encapsulation in hexagonal boron nitride (*h*-BN). *h*-BN also serves as an ideal substrate for graphene, due to its atomically flat surface and low lattice mismatch ($\sim$1.7%) [16] [Fig. 1(a)]. These lead to graphene heterostructures having outstanding electronic properties and large l_{diff}.

In recent years, hydrodynamic transport of charge has attracted significant theoretical attention [5,17–21], and several experimental signatures have been reported [6–8,22–25]. Of particular interest is the direct observation of the parabolic flow profile. Recent investigations utilizing direct imaging of Hall field [26] and local magnetic field [23,27] have hinted at the presence of viscous effects in charge transport in graphene and layered Weyl semimetals. Additionally, unique transport properties like formation of vortices, negative local resistance

and superballisticity have also been linked to a hydrodynamic charge flow [6,24,28]. Apart from the Coulomb mediated electron-electron interactions [5,17–20], recent reports also indicate the possibility of phonon mediated electronic interactions generating a correlated charge flow at higher carrier densities [27,28]. Though electrical signatures of Poiseuille flow in graphene have been reported [6,24], a comparative study of the transport signatures from multiple types of experiments and a determination of the temperature range for the viscous effects is lacking.

In the current work, we perform electrical transport measurements in *h*-BN encapsulated graphene field effect transistors (GrFETs) to investigate the presence of electronic Poiseuille flow. For this purpose, two separate measurement schemes are used: (1) current bias measurements (Sec. III) and (2) width-dependent measurements (Sec. IV). For the current bias measurements, we look into the scaling of channel resistance as a function of DC bias current in a sample of constant width [schematic in Fig. 2(a)]. The width-dependent measurements investigate the flow of charge carriers in channels of different widths [schematic in Fig. 3(a)]. We observe signatures of correlated charge flow for temperatures starting from $\sim$178 K and persisting upto 300 K. Further, finite element calculations are performed to verify the experimental observations (Sec. V). Our results demonstrate the presence of strong electronic correlations near room temperature opening up possibilities of utilizing the viscous electronic flow in graphene for functional devices.

II. ELECTRICAL PERFORMANCE OF GrFETS

The quality of the fabricated GrFETs was assessed by measuring the conductance of the channel as a function of gate voltage, as called a transfer characteristic at different temperatures [Fig. 1(b)]. The devices were fabricated using a standard dry transfer technique [29] and measurements performed in a four-probe geometry to remove the contact resistance (see Methods). *h*-BN encapsulation allows fabrication of edge contacts, which are known to outperform conventional surface contacts [30]. Figure 1(b) demonstrates a typical graphene transfer characteristic, with a maximum of resistance near the Dirac point and a sharp decrease with increasing number density (n). This corresponds to the transition from insulating behavior, caused by the formation of charge puddles near the neutrality point, to metallic behavior [31,32]. The high quality of our FETs is demonstrated by a large carrier mobility ($\mu \geqslant 2 \times 10^5$ cm^2/(Vs)) (Fig. S1 in Ref. [33]) and a large ł$_{\text{diff}} \geqslant 1$ μm [Fig. 1(c)], thereby relaxing the criteria for hydrodynamic behavior ($l_{ee} < l_{\text{diff}}, w$) for properly designed channels. The value of l_{diff} is computed considering a Drude model,

$$l_{\text{diff}} = \frac{\sigma m^* v_f}{n e^2},\qquad(1)$$

where σ is the channel conductivity, m^* the cyclotron mass [34], and $v_f = 10^6$ m s^{-1}, the Fermi velocity of graphene. We observe a reduction in the l_{diff} with increasing temperature (especially at $T = 337$ K), which can be attributed to increased momentum relaxing scattering events [16]. Temperature dependence of l_{diff} is provided in Fig. S1 [33].
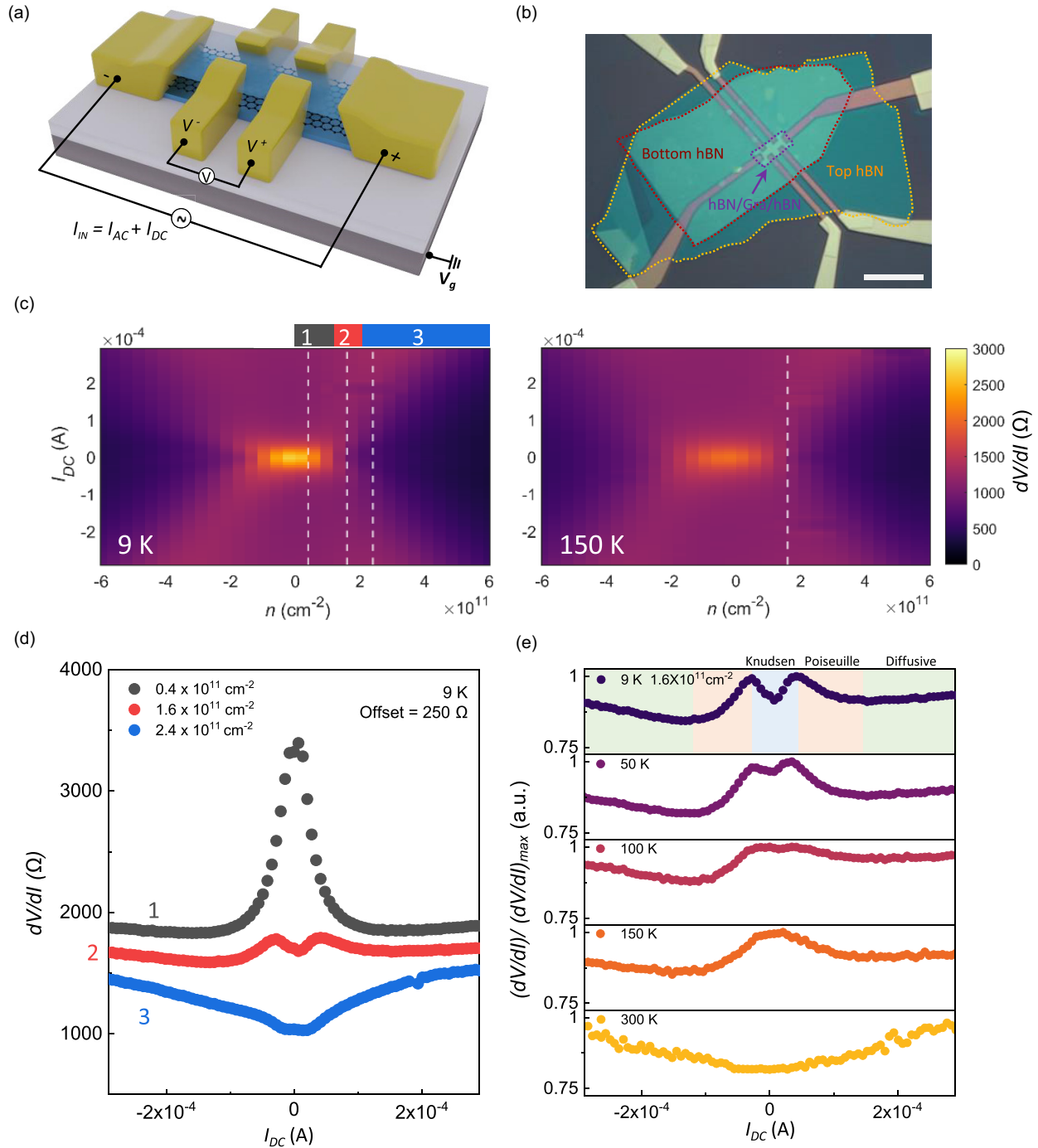
FIG. 2. Current bias measurements in GrFETs. (a) Schematic depiction of a typical GrFET device with circuit connections for current bias measurements. I_{AC} and I_{DC} represent the AC and DC bias current. V_g is the gate bias. (b) Optical image of the device used for current bias measurements. Red and yellow dot lines highlight the bottom and top h-BN flakes, respectively. The scale bar is 5 μm. (c) Color plots of dV/dI as a function of I_{DC} and n at $T = 9$ (left) and 150 K (right). (d) Plots depicting the I_{DC} dependence of differential resistance at $T = 9$ K for three different n values indicated by white dashed lines in (c). The number density ranges for the different dV/dI scaling behaviors are indicated at the top of the color plot (left panel in c) by solid lines of the same color as the corresponding scatter plot in (d). (e) Evolution of dV/dI curves at $n = 1.6 \times 10^{11}$ cm^{-2} (white dashed line for $T = 9$ and 150 K data in (c) for increasing values T from 9 (top) to 300 K (bottom). The Knudsen, Poiseuille, and diffusive transport regimes are indicated by color bars in the top panel.

III. CURRENT BIAS MEASUREMENTS

With the high quality of our GrFETs established, we turn to current bias measurements which consist of measuring the device conductance for increasing DC bias current. The role

of the DC bias ($|I_{DC}| \leqslant 300$ μA) is to increase the electronic temperature (T_e) of the devices, thereby providing a knob to increase the interparticles interactions and reduce l_{ee}. At the same time, the weak electron-phonon coupling in SLG ensures the lattice temperature does not significantly increase,
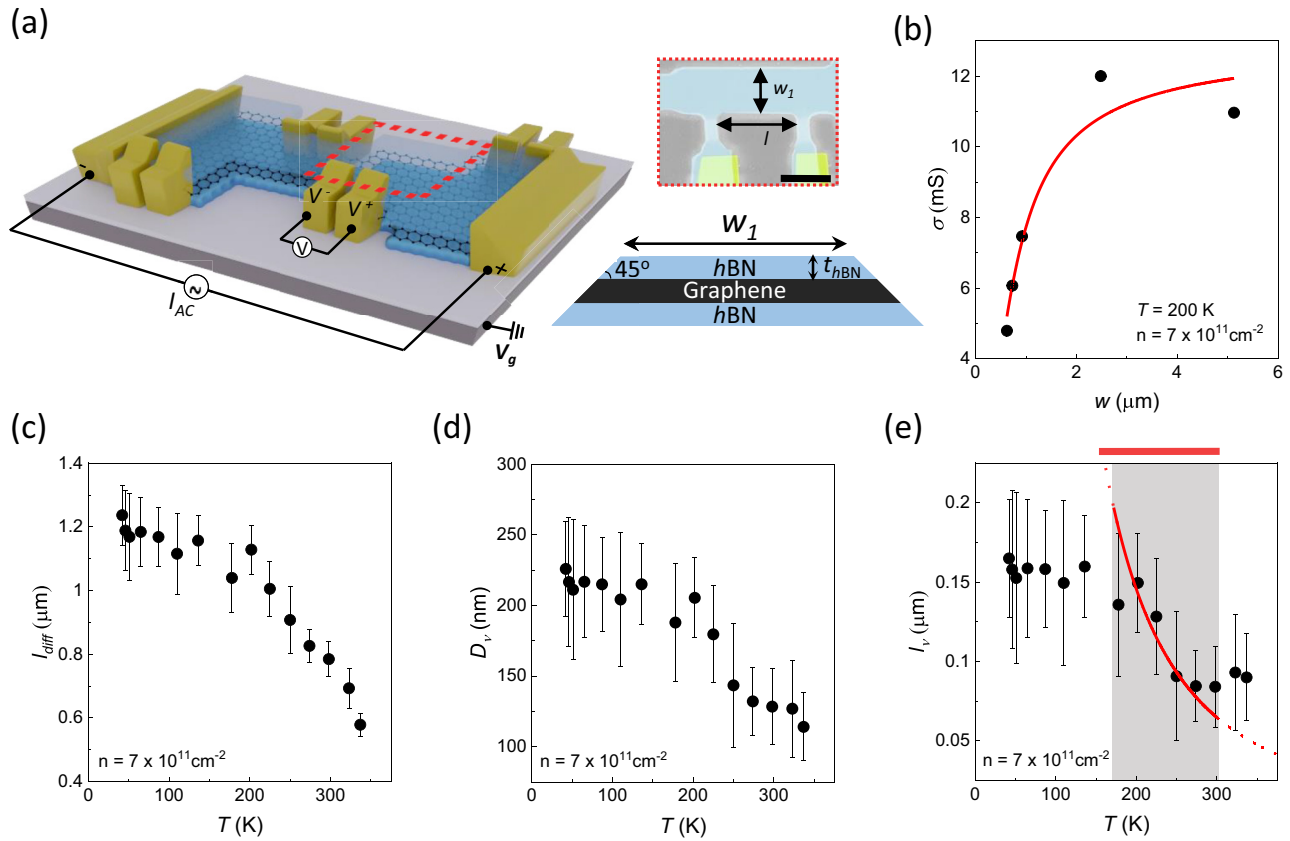
FIG. 3. Width-dependent measurements in GrFETs. (a) Left: schematic overview of GrFET design and circuit connection used for width-dependent measurements. Regions of different widths (w) are fabricated on the same heterostructure using EBL and RIE (see Methods). Top right: false colored scanning electron microscopy (SEM) image, used for measuring the channel dimensions. Scale bar is 1 μm. The SEM image is from a region depicted by a red dotted line in the left panel. Bottom right: schematic of the device cross-section depicting the correction introduced in the calculation of w due to the etching angle. (b) Scaling of σ as a function of w at $T = 200$ K. Solid line is a fit to the measured values (closed circles) following Eq. (5). (c), (d), and (e) represent l_{diff}, D_v, and l_v values, respectively, as a function of T, extracted from the fits in (b). Red line (both solid and dotted) and shaded region in e. represent theoretically predicted scaling of l_v, following Eq. (7) and the temperature range for Poiseuille effffects in GrFETs from width-dependent measurements, respectively. The red colored bar above (e) represents the temperature range for Poiseuille effects observed from the current bias measurements (Fig. 2 and Sec. III). Error bars in (c), (d), and (e) are calculated from the fitting error in (b).

which would lead to an increase in diffusive scattering processes, and hence a decrease in l_{diff} [13–15]. The decoupling of the two length scales therefore creates an ideal scenario for hydrodynamic charge flow [9]. We discuss the validity of this assumption below.

In the current work, we use I_{DC} to induce hot electrons in the GrFET. The dissipated power heats up the charge carriers and follows a I_{DC}^2 scaling. Following previous reports [35,36], we can calculate a value of $\Delta T_e \sim T_e - T \sim 200$ K (at $T = 9$ K), in the measured device. This is similar to values reported for graphene field effect transistors [6,36]. However, the lattice remains largely unaffected by I_{DC}. This was experimentally verified by measuring the shift in the 2D peak of graphene as a function of input bias voltage [36]. The authors of the aforementioned work report a 30 K/V increase in lattice temperature due to bias induced phonon heating. For the devices in the current work, this would correspond to a lattice temperature change of $\Delta T \sim 10.5$ K at $I_{\text{DC}} = 300\,\mu A$ (at $T = 9$ K). The value of ΔT is negligible when compared to $\Delta T_e \sim 200\,K$. Additionally, the bias induced phonon heating process shows negligible temperature dependence [36],

enabling an effective control of T_e for a wide range of temperatures using I_{DC}.

Figure 2(a) presents the device geometry and circuit connections used for the current bias measurements and Fig. 2(b) is an optical micrograph of the measured device. The measured device has a channel length and width of 1.1 and 0.55 μm, respectively. The transfer characteristics, mobility and l_{diff} of the device are presented in Fig. S2 [33]. Figure 2(c) shows color plots of dV/dI as a function of n and I_{DC} recorded at 9 and 150 K. At $T = 9$ K, for changing number densities, three types of I_{DC} curves are observed. The number densities in which these behaviors are observed are indicated above the color plot. For each behavior, a typical I_{DC} curve is plotted in Fig. 2(d), with the number densities highlighted by the vertical dashed lines in Fig. 2(c). For low n (scaling behavior 1), the dV/dI values follow a monotonic decreasing trend with increasing I_{DC} until about 5×10^{-5} A ($J_{\text{min}} \approx 0.09$ mA/μm). For larger values of I_{DC}, the curve is stable with only a minute increase in resistance. This behavior results in a central bright spot in the color map. With increasing n, we observe a non-monotonicity in the measured dV/dI, as apparent from the

central bright spot that splits into two ridges and a valley appearing in the center (scaling behavior 2).

For scaling behavior 2, the I_{DC} curves exhibit three distinct regions. First, for low DC currents, the dV/dI values increase with current. dV/dI then reaches a peak and in the second region, decreases for increasing current (reaching a minimum of dV/dI), while in the third region, dV/dI steadily increases with DC current. The experimentally observed nonmonotonicity in the differential resistance hints towards the presence of viscous effects [$n = 1.6 \times 10^{11}$ cm^{-2} in Fig. 2(d)], as we will discuss later on. Finally, for the largest n (scaling behavior 3), the negative slope region vanishes and the dV/dI is constant for small I_{DC} with a monotonic increase for higher current values.

The three different scaling behaviors with changing n can be rationalized as follows. For scaling behavior 1, electrical transport is dominated by the formation of charge puddles, leading to an insulating behavior at low DC currents, with a transition to metallic behavior for increasing DC current [31,32,37,38]. The initial drop in resistance is associated with electric field assisted interband carrier generation [37]. We can caluclate the charge inhomogeneity (Δn) near the Dirac point from the minima in the dV/dI. This gives $\Delta n = J_{min}/ev_f \approx 5 \times 10^{10}$ cm^{-2}, which is similar to those reported in encapsulated graphene [38]. The metallic behavior at higher I_{DC} has been attributed to a Schwinger production of electron hole plasma in graphene [38]. For scaling behavior 2, increasing the DC current leads to three distinct regions in the I_{DC} curve in which the charge transport is quasiballistic/Knudsen, hydrodynamic/Poiseuille and diffusive, respectively. For low DC currents, the charge carriers flow nearly collisionless, leading to a quasiballistic transport, also known as the electronic Knudsen regime. The transfer characteristics also indicate the presence of quasiballistic transport (Fig. S2 [33]) [39,40]. Upon increasing I_{DC}, the electron temperature increases and consequently the interparticle collisions are increased. Even though such collisions are momentum conserving and lead to no resistance, they make it more probable for the carriers to reach and diffusively interact with the sample boundaries [9], leading to an increase in the resistance [$d(dV/dI)/dI_{DC} > 0$]. A further increase in I_{DC} until $l_{ee} < w$ brings about a transition to the Poiseuille regime. Here, the interparticle collisions actively prevent a large fraction of the charge carriers (ones near the center of the channel) from seeing the boundaries, resulting in a slope reversal, $d(dV/dI)/dI_{DC} < 0$, and a minimum in the differential resistance. This negative slope for intermediate I_{DC} and minima of dV/dI in clean conductors are signatures of the electronic Gurzhi effect [41]. This has been experimentally observed previously and is indicative of the presence of viscous/Poiseuille flow [6,9]. This regime lasts until diffusive scattering processes within the sample gain prominence, restoring the positive slope of dV/dI as expected in standard metallic behavior or the diffusive regime (d(dV/dI)/$dI_{DC} > 0$). A similar behavior is observed in four different samples (see Methods for details). Finally, for higher number densities (scaling behavior 3), the interparticle interactions are screened (larger l_{ee}) [42,43] while the diffusive scattering remains largely unaffected [constant l_{diff} in Fig. S2 [33] and Fig. 1(c)] [6]. A combination of these effects leads to the vanishing of

the Poiseuille flow (negative slope of dV/dI). The dV/dI values are nearly constant for low I_{DC} (quasiballistic regime) and show an increasing trend once diffusive scattering starts dominating the transport around DC currents of 3×10^{-5} A (0.05 mA/μm). Similar observations were also made for hole transport in GrFETs (negative n), and are presented in Fig. S3 [33].

We also investigate the effect of the lattice temperature (T) on the Gurzhi effect by recording the conductance maps at different temperatures. The color plots at all temperatures are presented in Fig. S4 [33]. First, we compare the conductance map at 150 K [Fig. 2(c) (right panel)] to the one obtained at 9 K [Fig. 2(c) (left panel)]. Two major differences are observed. First, the central bright spot has a reduced intensity and, second, the Knudsen flow is absent for higher T values. Color plots at intermediate temperatures are presented in the Fig. S4 [33]. The reduction in intensity of the central bright spot is indicative of a reduced Dirac point resistance at higher values of T in GrFETs. This is an effect of the enhanced particle-hole excitation, similar to our observations in Fig. 1(b). The disappearance of the Knudsen regime is better visualized when the I_{DC} curves for an intermediate number density of $n = 1.6 \times 10^{11}$ cm^{-2} are investigated for all temperatures [Fig. 2(e)]. At low T, all three regimes, Knudsen, Poiseuille and diffusive are visible. However, with increasing T, the Knudsen regime first reduces in size, until it disappears at $T = 150$ K. Thereafter, at $T = 300$ K, the Poiseuille regime also vanishes and the GrFETs only demonstrate signatures of diffusive transport.

This T dependence can be understood by considering the variation of l_{ee} and l_{diff} with lattice temperature. At $T = 9$ K, l_{ee}, $l_{diff} \geqslant w$, which results in a quasiballistic or Knudsen flow persisting upto large values of I_{DC} (Fig. S2 [33]). A transition from Knudsen to Poiseuille flow occurs when $l_{ee} < w$. With increasing T, the Poiseuille flow condition is satisfied at smaller values of I_{DC}, leading to a diminishing Knudsen flow regime. This trend persists until the lattice temperature is high enough for the sample to enter the Poiseuille flow regime at $I_{DC} = 0$. This is indicated by the absence of the Knudsen regime and is observed at $T = 150$ K (Fig. S2 [33]). The sample remains in the Poiseuille regime until diffusive scattering processes gain prominence ($l_{diff} < l_{ee}$) and the differential resistance shows a monotonic positive slope [300 K data in Fig. 2(e)]. Our differential resistance measurements, thus, hint towards the presence of a viscous Poiseuille flow in GrFETs at temperatures between 150 and 300 K.

IV. WIDTH-DEPENDENT MEASUREMENTS

In addition to differential resistance measurements, we also verify the presence of Poisuille flow using geometric effects in the channel conductivity (σ). For diffusive transport, σ is a material parameter and therefore the current density (**J**) is uniform in the central part of the channel, vanishing at the boundaries, as shown in Ref. [23,26,44]. However, in the Poiseuille regime, the parabolic profile of **J** (or carrier velocity) [Fig. 1(a)] manifests itself as a strong width-dependence in σ. For a 2D Fermi liquid in the Poiseuille regime, the transport equations are given by [20]

$$\nabla \cdot \mathbf{J}(\mathbf{r}) = 0, \qquad (2)$$

$$\frac{\sigma_0}{e}\nabla\phi(r) + D_\nu^2\nabla^2\mathbf{J}(\mathbf{r}) = \mathbf{J}(\mathbf{r}), \qquad (3)$$

where Eqs. (2) and (3) are the electrical analogues of the continuity and Navier-Stokes equations, respectively. σ_0 is the Drude conductivity, $\phi(r)$ the electric potential and e the electronic charge. D_ν, the Gurzhi length, is a charcteristic length scale determining the strength of viscous effects. Its functional dependence is given by

$$D_\nu = \sqrt{\frac{\nu l_{\text{diff}}}{v_f}}, \qquad (4)$$

where ν is the kinematic viscosity. The second term of Eq. (3) is the viscous term and is responsible for the geometry dependence of σ. An analytical relation for σ is obtained by solving Eqs. (2) and (3) with a diffusive/no-slip boundary condition. Our choice of no-slip boundary condition follows from current profile imaging experiments in similar devices which demonstrate a decrease of the flow velocity near the channel boundaries [23,26,44]. The resulting functional dependence is

$$\sigma = \sigma_0\left[1 - 2\frac{D_\nu}{w}\tanh\left(\frac{w}{2D_\nu}\right)\right]. \qquad (5)$$

From Eq. (5), we can define an asymptotic limit of strong Poiseuille flow using the condition $D_\nu \gg w$. In this case, we obtain, $\sigma = \sigma_0 w^2/12D_\nu$. This w^2 scaling of σ has been reported previously in the Fermi liquid of Weyl semimetals [8]. However, comparing the values of w used in the current work ($0.6 < w < 5\,\mu$m) and previously reported values of $D_\nu \approx$ 0.2–0.4 μm in graphene [6], we expect that the measured GrFETs do not satisfy the conditions for strong Poiseuille flow. Hence, unlike previous reports [8], we find it suitable to fit the experimental σ with the nonasymptotic relation given by Eq. (5).

Figure 3(a) shows a schematic of the GrFETs used for our width-dependent measurements. To fabricate these devices, the h-BN encapsulated graphene heterostructure was shaped into channels of different widths using reactive ion etching (RIE) (see Methods). Channel widths (w_1) and lengths (l) were confirmed by scanning electron micrographs [top right panel of Fig. 3(a)]. The actual channel width (w) was estimated from the observed width (w_1), plus taking into consideration the height of the top h-BN and the 45° angle generated by the RIE process [bottom right panel of Fig. 3(a)] [30]. The width-dependent fitting allows us to extract several flow parameters, providing further insight into the viscous charge transport in GrFETs. A detailed discussion of the process is presented below.

The transfer characteristic and l_{diff} of the width-dependent device is presented in Figs. 1(b) and 1(c), respectively. Figure 3(b) shows the fitting of σ for lattice temperature $T = 200$ K and $n = 7 \times 10^{11}$ cm^{-2}. This particular choice of T and n is guided by previous reports of viscous effects in graphene at similar values of these parameters [6]. The closed circles are measured values of σ, while the solid line is a fit following Eq. (5), with σ_0 and D_ν as fitting parameters. From the fit, one can directly extract the values of σ_0 and D_ν. The extracted value of σ_0 enables us to compute the diffusive mean free path

l_{diff} using Eq. (1). We find $l_{\text{diff}} \sim 1\,\mu$m, which is a common occurrence in high quality graphene devices [Fig. 3(c)] [6,30]. The value of $D_\nu \sim 0.2\,\mu$m [Fig. 3(d)], obtained from the fit is also in close agreement with previous reports [6]. Substituting l_{diff} and D_ν in Eq. (4) gives us an estimate of the viscosity (ν) of the charge carriers. We obtain a high kinematic viscosity, $\nu \approx 0.04\,\text{m}^2\text{s}^{-1}$ ($T = 200$ K), making the flow more viscous than honey, a phenomenon which has been reported previously (Fig. S5 [33]) [6]. This high viscosity is also one of the assumptions for using the linearized Navier-Stokes equation in Eq. (3). Additionally, the flow viscosity, which arises due to the interparticle scattering, can be directly related to the viscous mean free path, l_ν, a parameter which is closely related to l_{ee} [6,19]. The exact relationship at low excitation frequencies ($f << 10^{12}$ Hz) is given by

$$l_\nu = \frac{4m^*\nu}{\hbar k_f}. \qquad (6)$$

The extracted $l_\nu \approx 0.14\,\mu$m at $T = 200$ K, is the smallest length scale in the system ($l_\nu << w, l_{\text{diff}}$), indicative of the presence of Poiseuille flow in GrFETs at $T = 200$ K [Fig. 3(e)]. To explore further, we repeat the width-dependent measurements at different lattice temperatures and explore the temperature dependence of l_{diff}, D_ν, l_ν, and ν in Figs. 3(c)–3(e), and Fig. S5 [33], respectively. The flow parameters demonstrate a T dependence only in an intermediate temperature range of $178 < T < 300$ K and saturate (except for l_{diff}) for $T < 178$ K and $T > 300$ K.

To understand the physical relevance of these values, we compare the extracted l_ν with its predicted T dependence for the Dirac fermionic liquid in a doped graphene sheet [19]. The analytical relation for l_ν is given by

$$l_\nu = \frac{45v_f(1 + N_f\alpha_{ee})^2\hbar\epsilon_f}{64\pi\sqrt{2}N_f\alpha_{ee}^2(k_BT)^2}, \qquad (7)$$

where $N_f = 4$ is the number of Fermionic flavours in graphene, $\alpha_{ee} = 7.3$ the fine structure constant, and k_B the Boltzmann constant. α_{ee} is computed from the relation [19,45]

$$\alpha_{ee} = \frac{e^2}{\epsilon\hbar v_f}, \qquad (8)$$

where ϵ is the electrical permittivity. For the current work, we have used the permittivity of h-BN considering a dielectric constant of 4 [46]. Eq. (7) [solid line in Fig. 3(e)] has no fitting parameters and matches the extracted values of l_ν [closed circles in Fig. 3(e)] for the intermediate temperature range, $178 < T < 300$ K [shaded region in Fig. 3(e)]. The extracted flow parameters are thus physically relevant only for these intermediate temperatures. Additionally, we note that the assumptions of viscous flow made in the formulation of the transport equations [Eqs. (2) and (3)] limit their validity, and as a result, the validity of the geometry-dependent analysis for values of T where Poiseuille flow is present. In combination, the physical relevance of the extracted flow parameters and the validity of the viscous flow equations confirm the presence of Poiseuille flow for $178 < T < 300$ K in GrFETs. Finally, this observation is strengthened by the fact that similar T values are obtained for both the current bias measurements (Sec. III) and width-dependent measurements [Figs. 2(e) and
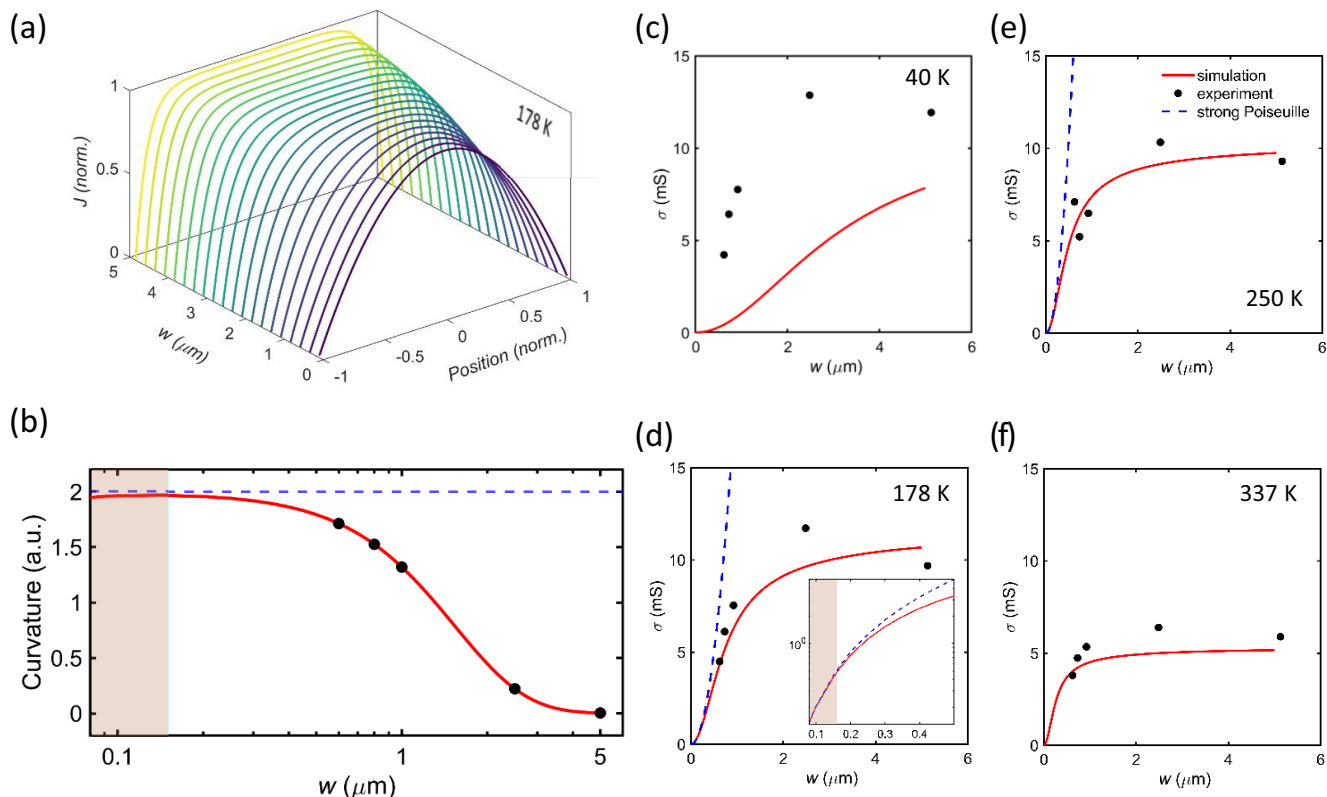
FIG. 4. Finite element modeling of graphene channel. (a) Plots of J_{norm} as a function of w and *Position* (*norm.*) at $T = 178$ K depicting a parabolic current flow profile for small values of w and a uniform J_{norm} for the largest simulated widths. (b) Flow curvature (solid line) as a function of w computed from flow profiles in (a) at *Position* (*norm.*) $= 0$. Filled circles indicate the curvatures for measured values of w in the current work. The dashed line represents curvature for an ideal parabolic flow. Shaded region indicates w values for strong Poiseuille flow (from inset of (d). [(c), (d), (e), and (f)] Experimental (filled circles) and simulated (solid line) values of σ as a function of w for $T = 40, 178, 250$, and 337 K, respectively. Dashed line in (d) and (e) indicates the w^2 scaling of σ expected for strong Poiseuille effects. Inset of (d) compares the w^2 scaling and simulated σ for $w \leqslant 0.5 \, \mu$m. Shaded region represents the predicted w values for strong Poiseuille flow. The finite element modeling is performed at $n = 7 \times 10^{11}$ cm^{-2}.

3(e)]. We also look at the number density dependence of the flow parameters in Fig. S6 [33]. The geometry-dependent measurements indicate the presence of hydrodynamic effects for number densities $>10^{11}$ cm^{-2}. Further discussions are provided in Fig. S6 [33].

V. FINITE ELEMENT METHODS

Finally, we turn to finite element calculations (implemented in COMSOL MULTIPHYSICS 5.6) to model the Poiseuille flow in GrFETs. This process involves numerically solving Eqs. (2) and (3) with an uniform electric field ($\nabla \phi$) and no-slip boundary conditions for different values of w. The input parameters, D_ν and σ_0, are calculated from the theoretical predictions of l_ν [Eq. (7)] and the field effect mobility (μ). Our channels are oriented along the x axis while their width follows the y axis. An example of a simulated flow profile is depicted in Fig. 4(a) for $T = 178$ K. We observe strong Poiseuille effects for small channel widths, indicated by the parabolic dependence of the normalized current density $[J_{\text{norm}} = J_x(y)/J_x(y = 0)]$ on the normalized channel position [*Position* (*norm.*) $= y/(w/2)$], and a weak Poiseuille flow, indicated by a constant J_{norm}, for larger values of w. The curvature of the flow profile computed at the center of the

channel [*Position* (*norm.*) $= 0$] also exhibits a width dependence [solid line in Fig. 4(b)]. It saturates to a value of 2 for the smallest widths with a parabolic flow profile [$w = 0.1 \, \mu$m in Fig. 4(a)] and reduces to 0 for larger widths with a constant J_{norm} [$w = 5 \, \mu$m in Fig. 4(a)]. The filled circles in Fig. 4(b) correspond to the measured values of w in the current work. Further, we extract the channel conductivity (σ) from the simulated flow profile. In Figs. 4(c) to 4(f), the simulated (solid red line) and experimental (filled circles) values of σ are compared for four different values of T. The simulated results match experimental data for temperatures in the Poiseuille flow regime ($T = 178$ and 250 K), with mismatches at lower ($T = 40$ K) and higher ($T = 337$ K) temperatures, where our experiments indicate the absence of hydrodynamic effects.

In what follows, we quantify our observations and predict the values of w necessary for a strong Poiseuille flow. As discussed before, the strong Poiseuille regime is characterized by a w^2 scaling of σ. This is indicated by the dashed blue lines in Figs. 4(d) and 4(e), computed with the same parameter values as in the simulation (solid red line). Indeed, the experimentally measured widths in our GrFETs devices are too large for observing this effect as the flow is in the weak Poiseuille regime. The strong Poiseuille regime is determined by computing the relative difference between the simulated

(solid red line) and strong Poiseuille (dashed blue line) values of σ. Values of w for which the relative difference remains below 10% are considered to be in the strong Poiseuille regime. The criteria is satisfied for $w < 0.15\,\mu\text{m}$, indicated by the shaded region in the inset of Fig. 4(d). Another indicator of the strong Poiseuille regime is the saturation of the flow curvature to a value of 2 [shaded region in Fig. 4(b)]. In conclusion, our finite element model confirms our GrFETs are in the weak Poiseuille regime and predicts strong Poiseuille flow for $w < 0.15\,\mu\text{m}$ in GrFETs. Comparing the measured values of l_v [Fig. 3(e)] with the computed length scale for strong hydrodynamics, we would expect this behavior to be present at a slightly higher temperature than the range indicated in the current work in order to satisfy the criteria $l_{ee} < w$.

VI. DISCUSSIONS AND CONCLUSIONS

Fabrication related constraints, specifically, the availability of sizes of exfoliated graphene and h-BN flakes, governed the design of the width-dependent device measured in the current work. The design, presented in Fig. S10 [33], was adopted to increase the number of widths in a single graphene flake. This led to a variation in the aspect ratio of the channels in the regions of different widths. Notably, for the two largest measured widths, the separation between the voltage probes ($\sim 1.5\,\mu\text{m}$) is smaller than $w \sim 2.5$ and $5\,\mu\text{m}$, making the channel length, the smallest geometric length scale. To investigate the consequences of such a design choice, we simulate the flow profile in the measured device and compare it with that of a model geometry (Fig. S10 [33]). The geometry of the measured device is obtained from the gds file used to shape the device during fabrication. The model geometry is obtained by modifying the measured device and increasing the length of the segments with the largest widths (i.e., $w = 2.5$ and $5\,\mu\text{m}$). Comparing the flow profiles in the two geometries we find no difference for the smallest measured widths ($w = 0.6, 0.8$ and $1\,\mu\text{m}$), and a slight variation for the two largest widths (Fig. S10(c) [33]). The variation in the flow profile leads to a variation in the channel conductivity $\Delta\sigma \sim 7 - 15\%$ for $w = 2.5$ and $5\,\mu\text{m}$ when compared to the model geometry. While these values are not negligible, the extracted flow parameters from the model geometry fall within the variation introduced by the width-dependent fitting (demonstrated by error bars in Figs. 3(c)–3(e) and hence do not modify the conclusions drawn in the current work.

Additionally, we also investigate the injection effects that arise due to the connection of channels of different widths. This is done by extracting the flow profile at various regions in the channel (details in Fig. S11 [33]). We find negligible injection effects in the smallest measured widths ($w = 0.6$, 0.8, and $1\,\mu\text{m}$) (Fig. S11(b) [33]). We observe some injection effects in the largest measured widths, but these flow instabilities die down within 300 nm of the voltage probes and the flow in the majority of the measured channel is stable (although with a slight variation from the model geometry as mentioned previously) (Fig. S11(c) [33]). This makes us believe that the charge injection effects do not play a major role in the measured device. All the simulations are performed

at $T = 178$ K and $n = 7 \times 11$ cm^{-2}, following similar considerations as present in the discussion of Sec. V in the main text.

Strikingly, we observe hydrodynamic effects at different charge number densities in the geometry dependence study ($n > 1 \times 10^{11}$ cm^{-2}) (Fig. S6 [33]) and the current bias measurements ($1.6 \times 10^{11} \lesssim n \lesssim 2.4 \times 10^{11}$ cm^{-2}), for which we have no clear, unique explanation. Similar behavior has been seen in previous reports, with current bias measurements showing viscous effects for lower number density ranges compared to negative vicinity resistance [6]. This could indicate either a number density selectivity in the transport probes of charge hydrodynamics or a number density variability of the hydrodynamic regime in graphene.

In conclusion, we demonstrate the electrical signatures of Poiseuille flow in charge transport through graphene channels using the Gurzhi effect and geometry-dependent measurements. We observe a negative slope in the differential resistance measurements and a strong geometry dependence of the channel conductivity, both indicative of the presence of viscous effects. The two different measurements types, in conjunction, enable us to define a temperature range for the viscous effects to occur, which reaches as high as 300 K. Moreover, we provide an electrical transport-based characterization framework for detecting Poiseuille flow in conductors that can easily be extended to other conductors. Our experimental observations are corroborated by finite-element calculations that shed light on the channel geometries required for a strong Poiseuille flow. Our findings offer promising prospects for functional hydrodynamic graphene devices in the near future, such as geometric rectifiers like Tesla valves and charge amplifiers based on the electronic Venturi effects [47–49].

VII. METHODS

A. Device fabrication

GrFETs measured in the current work are fabricated using the following process: the heterostructure assembly begins with the mechanical exfoliation of individual layers from bulk crystals (the graphite is obtained commercially from NGS Trading & Consulting GmbH and the h-BN is from our coauthors in National Institute for Materials Science, Japan). Exfoliated flakes are optically screened using an optical microscope (Zeiss Axio Imager M2m). The layer number and quality of grphene flakes are determined using Raman spectroscopy (see Fig. S7 [33]) [50]. We use a Raman system with a backscattering geometry confocal Raman microscope (WITec, Alpha 300 R). An excitation laser with a wavelength of 532 nm from a diode laser is used for all Raman measurements. The thickness of h-BN layers is characterized using atomic force microscopy in the tapping mode (Bruker Icon3 AFM). Selected flakes are aligned and stacked layer by layer using commercially available micromanipulator (HQ Graphene 2D Heterostructure Transfer System). The pick-up process is performed using PDMS backed polycarbonate (PC) stamps. PC shows good adherence to h-BN for $330\,\text{K} \leqslant T \leqslant 350$ K. After successful pick-up of the top h-BN layer, the middle graphene layer and bottom h-BN layer are picked up using the van der Waals interaction between the different two-dimensional materials. Finally, the heterostructure is

deposited on a pre-patterned Si^{++}/SiO_2 (285 nm) wafer at $T = 450$ K. The PC is dissolved in dchlorometane (DCM). The transfer process followed is similar to that in Ref. [29]. Following this, a thermal annealing step is performed at 650 K with H_2/Ar 35/200 sccm for 3 hours to improve the quality of the heterostructures by reducing interfacial bubbles, contaminants etc. (See Figs. S8 and S9 [33].) The small electrodes are defined using EBL and RIE ($CHF_3 = 40$ sccm, $O_2 = 4$ sccm, $P = 60$ mTorr, Power $= 60$ W). Next, we deposit 5/25 nm Cr/Au directly using ebeam evaporator for edge-contacted electrodes and the pattern is lifted off using acetone for 45 min [30]. After that, the second EBL and metals deposition (5/65 nm Cr/Au) are performed for contact pads. Finally, we perform the third ebeam processing, followed by the second RIE for defining the channel shape. The morphology of the device is recorded by the same optical microscope mentioned above. Channel widths of devices are acquired from SEM (Hitachi S-4800). For the width-dependent device the channel width (w) was varied while keeping the channel length constant.

For the current bias measurements, four devices on four different chips were fabricated. All samples demonstrate a similar scaling of dV/dI at base temperature. We observe the current biasing measurements have a tendency to generate irreversible hysteresis and electron doping (shifting of the Dirac point to negative gate voltages) in devices. Due to this we could perform the temperature characterization in one device and partial temperature characterization in a second device.

For the width-dependent measurements, the largest four values of w are from a single large graphene channel which was shaped into channels of different widths, while the smallest w value is obtained from a second device on a different chip made following similar fabrication protocols.

B. Measurement Details

The four-probe resistance of GrFETs was measured using a lock-in technique, with an AC source-drain current(of $I_{AC} = 100$ nA (231.45 Hz); $I_{DC} = 0$) while measuring the resulting voltage drop (Lockins used are SRS 830 or EG&G 7265). The SRS CS580 voltage controlled current source is used to supply I_{AC} to the sample. The gate voltage is supplied by an AdWin Gold 2 connected to a voltage amplifier (Physics Basel SP 908). From the applied gate voltage, the number density is computed using $n = C_{ox}(V_g - V_d)/e$ [51], where, C_{ox} is the oxide capacitance (series combination of SiO_2 (285 nm) and bottom h-BN), e is the electron charge, V_g and V_d are the gate and the Dirac point voltage, respectively.

For the current bias measurements, the DC bias is supplied by an AdWin Gold 2 and the AC bias by a lockin. The two bias voltages are added using a summing amplifier SIM980. The current source CS580 converts the summed voltage to the supplied current bias. An $I_{AC} = 100$ nA (231.5 Hz) is used for the measurements and the output voltage from the sample measured using the lockin.

The width-dependent measurements follow similar measurement technique as the transfer characteristic measurements.

The current bias measurements are carried out on a closed cycle manual probe station (Lakeshore). For width dependence measurements, the samples are wire bonded to a chip carrier and measured in a commercially available closed cycle cryostat from Advanced Research Systems (ARS).

The data that support the findings of the study are available from the corresponding author upon reasonable request.

ACKNOWLEDGMENTS

W.H., T.P., M.L.P., and M.C. conceived and designed the experiments. W.H. and T.P. prepared the devices and performed the electrical measurements. W.H. and T.P. performed the annealing, Raman, SEM and AFM measurements. K.W. and T. T. synthesized the hBN flakes. W.H., T.P., M.L.P., and M.C. did the data analysis. M.L.P. performed the finite element calculations, with the help of T.P., W.H., T.P., M.L.P., and M.C. discussed the figures and wrote the manuscript. M.L.P. and M.C. supervised the study. All authors discussed the results and implications and commented on the manuscript.

The authors declare that there are no competing interests.

[1] N. W. Ashcroft and N. D. Mermin, *Solid State Physics* (Holt, Rinehart and Winston, New York London, 1976).

[2] S. Datta, *Electronic Transport in Mesoscopic Systems* (Cambridge University Press, 1997).

[3] L. D. Landau and E. M. Lifshitz, *Fluid Mechanics*, Course of Theoretical Physics Vol. 6 (Elsevier, 2013).

[4] C. K. Batchelor and G. Batchelor, *An Introduction to Fluid Dynamics* (Cambridge university press, 2000).

[5] D. Y. H. Ho, I. Yudhistira, N. Chakraborty, and S. Adam, Theoretical determination of hydrodynamic window in monolayer and bilayer graphene from scattering rates, Phys. Rev. B **97**, 121404(R) (2018).

[6] D. Bandurin, I. Torre, R. K. Kumar, M. B. Shalom, A. Tomadin, A. Principi, G. Auton, E. Khestanova, K. Novoselov, I. Grigorieva, L. A. Ponomarenko, A. K. Geim, and M. Polini, Negative local resistance caused by viscous electron backflow in graphene, Science **351**, 1055 (2016).

[7] P. J. Moll, P. Kushwaha, N. Nandi, B. Schmidt, and A. P. Mackenzie, Evidence for hydrodynamic electron flow in PdCoO$_2$, Science **351**, 1061 (2016).

[8] J. Gooth, F. Menges, N. Kumar, V. Süß, C. Shekhar, Y. Sun, U. Drechsler, R. Zierold, C. Felser, and B. Gotsmann, Thermal and electrical signatures of a hydrodynamic electron fluid in tungsten diphosphide, Nat. Commun. **9**, 4093 (2018).

[9] M. J. M. de Jong and L. W. Molenkamp, Hydrodynamic electron flow in high-mobility wires, Phys. Rev. B **51**, 13389 (1995).

[10] A. C. Keser, D. Q. Wang, O. Klochan, D. Y. H. Ho, O. A. Tkachenko, V. A. Tkachenko, D. Culcer, S. Adam, I. Farrer, D. A. Ritchie, O. P. Sushkov, and A. R. Hamilton, Geometric Control of Universal Hydrodynamic Flow in a Two-Dimensional Electron Fluid, Phys. Rev. X **11**, 031030 (2021).

[11] A. K. Geim and A. H. MacDonald, Graphene: Exploring carbon flatland, Phys. Today **60**(8), 35 (2007).

[12] R. Roldán, M. P. López-Sancho, and F. Guinea, Effect of electron-electron interaction on the fermi surface topology of doped graphene, Phys. Rev. B **77**, 115410 (2008).

[13] J. C. Johannsen, S. Ulstrup, M. Bianchi, R. Hatch, D. Guan, F. Mazzola, L. Hornekær, F. Fromm, C. Raidel, T. Seyller, *et al.*, Electron–phonon coupling in quasi-free-standing graphene, J. Phys.: Condens. Matter **25**, 094001 (2013).

[14] C. Si, Z. Liu, W. Duan, and F. Liu, First-Principles Calculations on the Effect of Doping and Biaxial Tensile Strain on Electron-Phonon Coupling in Graphene, Phys. Rev. Lett. **111**, 196802 (2013).

[15] M. Calandra and F. Mauri, Electron-phonon coupling and electron self-energy in electron-doped graphene: Calculation of angular-resolved photoemission spectra, Phys. Rev. B **76**, 205411 (2007).

[16] C. R. Dean, A. F. Young, I. Meric, C. Lee, L. Wang, S. Sorgenfrei, K. Watanabe, T. Taniguchi, P. Kim, K. L. Shepard, and J. Hone, Boron nitride substrates for high-quality graphene electronics, Nat. Nanotechnol. **5**, 722 (2010).

[17] F. M. D. Pellegrino, I. Torre, A. K. Geim, and M. Polini, Electron hydrodynamics dilemma: Whirlpools or no whirlpools, Phys. Rev. B **94**, 155414 (2016).

[18] D. Svintsov, Hydrodynamic-to-ballistic crossover in dirac materials, Phys. Rev. B **97**, 121405(R) (2018).

[19] A. Principi, G. Vignale, M. Carrega, and M. Polini, Bulk and shear viscosities of the two-dimensional electron liquid in a doped graphene sheet, Phys. Rev. B **93**, 125410 (2016).

[20] I. Torre, A. Tomadin, A. K. Geim, and M. Polini, Nonlocal transport and the hydrodynamic shear viscosity in graphene, Phys. Rev. B **92**, 165433 (2015).

[21] M. Chandra, G. Kataria, D. Sahdev, and R. Sundararaman, Hydrodynamic and ballistic ac transport in two-dimensional fermi liquids, Phys. Rev. B **99**, 165409 (2019).

[22] D. A. Bandurin, A. V. Shytov, L. S. Levitov, R. K. Kumar, A. I. Berdyugin, M. Ben Shalom, I. V. Grigorieva, A. K. Geim, and G. Falkovich, Fluidity onset in graphene, Nat. Commun. **9**, 4533 (2018).

[23] M. J. Ku, T. X. Zhou, Q. Li, Y. J. Shin, J. K. Shi, C. Burch, L. E. Anderson, A. T. Pierce, Y. Xie, A. Hamo, *et al.*, Imaging viscous flow of the dirac fluid in graphene, Nature (London) **583**, 537 (2020).

[24] R. K. Kumar, D. Bandurin, F. Pellegrino, Y. Cao, A. Principi, H. Guo, G. Auton, M. B. Shalom, L. A. Ponomarenko, G. Falkovich, *et al.*, Superballistic flow of viscous electron fluid through graphene constrictions, Nat. Phys. **13**, 1182 (2017).

[25] E. Mönch, S. O. Potashin, K. Lindner, I. Yahniuk, L. E. Golub, V. Y. Kachorovskii, V. V. Bel'kov, R. Huber, K. Watanabe, T. Taniguchi, *et al.*, Ratchet effect in spatially modulated bilayer graphene: Signature of hydrodynamic transport, Phys. Rev. B **105**, 045404 (2022).

[26] J. A. Sulpizio, L. Ella, A. Rozen, J. Birkbeck, D. J. Perello, D. Dutta, M. Ben-Shalom, T. Taniguchi, K. Watanabe, T. Holder, *et al.*, Visualizing poiseuille flow of hydrodynamic electrons, Nature (London) **576**, 75 (2019).

[27] U. Vool, A. Hamo, G. Varnavides, Y. Wang, T. X. Zhou, N. Kumar, Y. Dovzhenko, Z. Qiu, C. A. Garcia, A. T. Pierce, *et al.*, Imaging phonon-mediated hydrodynamic flow in WTe$_2$, Nat. Phys. **17**, 1216 (2021).

[28] A. Aharon-Steinberg, T. Völkl, A. Kaplan, A. K. Pariari, I. Roy, T. Holder, Y. Wolf, A. Y. Meltzer, Y. Myasoedov, M. E. Huber, B. Yan, G. Falkovich, L. S. Levitov, M. Hücker, and E. Zeldov, Direct observation of vortices in an electron fluid, Nature (London) **607**, 74 (2022).

[29] P. Zomer, M. Guimarães, J. Brant, N. Tombros, and B. Van Wees, Fast pick up technique for high quality heterostructures of bilayer graphene and hexagonal boron nitride, Appl. Phys. Lett. **105**, 013101 (2014).

[30] L. Wang, I. Meric, P. Huang, Q. Gao, Y. Gao, H. Tran, T. Taniguchi, K. Watanabe, L. Campos, D. Muller, J. Guo, P. Kim, J. Hone, K. L. Shepard, and C. R. Dean, One-dimensional electrical contact to a two-dimensional material, Science **342**, 614 (2013).

[31] J. Martin, N. Akerman, G. Ulbricht, T. Lohmann, J. v. Smet, K. Von Klitzing, and A. Yacoby, Observation of electron–hole puddles in graphene using a scanning single-electron transistor, Nat. Phys. **4**, 144 (2008).

[32] J. Xue, J. Sanchez-Yamagishi, D. Bulmash, P. Jacquod, A. Deshpande, K. Watanabe, T. Taniguchi, P. Jarillo-Herrero, and B. J. LeRoy, Scanning tunnelling microscopy and spectroscopy of ultra-flat graphene on hexagonal boron nitride, Nat. Mater. **10**, 282 (2011).

[33] See Supplemental Material at http://link.aps.org/supplemental/10.1103/PhysRevResearch.5.023075 for device characterization, number density dependence of flow parameters and a discussion on charge injection effects.

[34] A. H. CastroNeto, F. Guinea, N. M. R. Peres, K. S. Novoselov, and A. K. Geim, The electronic properties of graphene, Rev. Mod. Phys. **81**, 109 (2009).

[35] J. D. Crossno, Electronic Thermal Conductance of Graphene via Electrical Noise, Ph.D. thesis, Harvard University (2017).

[36] A. C. Betz, F. Vialla, D. Brunel, C. Voisin, M. Picher, A. Cavanna, A. Madouri, G. Fève, J.-M. Berroir, B. Plaçais, *et al.*, Hot Electron Cooling by Acoustic Phonons in Graphene, Phys. Rev. Lett. **109**, 056805 (2012).

[37] N. Vandecasteele, A. Barreiro, M. Lazzeri, A. Bachtold, and F. Mauri, Current-voltage characteristics of graphene devices: Interplay between Zener-Klein tunneling and defects, Phys. Rev. B **82**, 045416 (2010).

[38] A. I. Berdyugin, N. Xin, H. Gao, S. Slizovskiy, Z. Dong, S. Bhattacharjee, P. Kumaravadivel, S. Xu, L. Ponomarenko, M. Holwill, *et al.*, Out-of-equilibrium criticalities in graphene superlattices, Science **375**, 430 (2022).

[39] B. Terrés, L. Chizhova, F. Libisch, J. Peiro, D. Jörger, S. Engels, A. Girschik, K. Watanabe, T. Taniguchi, S. Rotkin, *et al.*, Size quantization of dirac fermions in graphene constrictions, Nat. Commun. **7**, 11528 (2016).

[40] B. J. van Wees, H. van Houten, C. W. J. Beenakker, J. G. Williamson, L. P. Kouwenhoven, D. van der Marel, and C. T. Foxon, Quantized Conductance of Point Contacts in a Two-Dimensional Electron Gas, Phys. Rev. Lett. **60**, 848 (1988).

[41] R. Gurzhi, Minimum of resistance in impurity-free conductors, J. Exptl. Theoret. Phys. **44**, 771 (1963).

[42] G. Giuliani and G. Vignale, *Quantum Theory of the Electron Liquid* (Cambridge University Press, 2005).

[43] M. Razeghi, *Fundamentals of Solid State Engineering* (Springer, 2006).

[44] L. Ella, A. Rozen, J. Birkbeck, M. Ben-Shalom, D. Perello, J. Zultak, T. Taniguchi, K. Watanabe, A. K. Geim, S. Ilani, *et al.*, Simultaneous voltage and current density imaging of flowing electrons in two dimensions, Nat. Nanotechnol. **14**, 480 (2019).

[45] V. N. Kotov, B. Uchoa, V. M. Pereira, F. Guinea, and A. H. CastroNeto, Electron-electron interactions in graphene: Current status and perspectives, Rev. Mod. Phys. **84**, 1067 (2012).

[46] K. K. Kim, A. Hsu, X. Jia, S. M. Kim, Y. Shi, M. Dresselhaus, T. Palacios, and J. Kong, Synthesis and characterization of hexagonal boron nitride film as a dielectric layer for graphene devices, ACS Nano **6**, 8583 (2012).

[47] D. Taubert, G. J. Schinner, C. Tomaras, H.-P. Tranitz, W. Wegscheider, and S. Ludwig, An electron jet pump: The venturi effect of a fermi liquid, J. Appl. Phys. **109**, 102412 (2011).

[48] D. Taubert, G. J. Schinner, H. P. Tranitz, W. Wegscheider, C. Tomaras, S. Kehrein, and S. Ludwig, Electron-avalanche amplifier based on the electronic venturi effect, Phys. Rev. B **82**, 161416(R) (2010).

[49] M. Szelong, A. Ludwig, A. D. Wieck, and U. Kunze, Positive centre voltage in t-branch junctions on n-type GaAs/AlGaAs based on hydrodynamics, Semicond. Sci. Technol. **32**, 105005 (2017).

[50] A. C. Ferrari, J. C. Meyer, V. Scardaci, C. Casiraghi, M. Lazzeri, F. Mauri, S. Piscanec, D. Jiang, K. S. Novoselov, S. Roth, *et al.*, Raman Spectrum of Graphene and Graphene Layers, Phys. Rev. Lett. **97**, 187401 (2006).

[51] K. S. Novoselov, A. K. Geim, S. V. Morozov, D. Jiang, Y. Zhang, S. V. Dubonos, I. V. Grigorieva, and A. A. Firsov, Electric field effect in atomically thin carbon films, Science **306**, 666 (2004).